ADVANCED FUNCTIONAL MATERIALS
www.afm-journal.de

Enhanced Incorporation of Guanidinium in Formamidinium-Based Perovskites for Efficient and Stable Photovoltaics: The Role of Cs and Br

Yang Zhou, Haibo Xue, Yong-Heng Jia, Geert Brocks, Shuxia Tao, and Ni Zhao**

Recently, incorporating guanidium (GA) cations into organolead halide perovskites is shown to effectively improve the stability and performance of the solar cells. However, the underlying mechanisms that govern the GA incorporation have remained unclear. Here, $FAPbI_3$ is used as a basic framework to investigate experimentally and theoretically the role of cesium (Cs) and bromine (Br) substitutions in GA^+ incorporation. It is found that simultaneous introduction of the small-size Cs^+ and Br^- in the $FAPbI_3$ lattice is critical to create sufficient space for the large GA^+ and that the presence of the Cs^+ prevents the formation of a GA-contained low-dimensional phase, which both assist GA^+ incorporation. Upon entering the perovskite lattice, the GA^+ can stabilize the lattice structure via forming strong hydrogen bonds with their neighboring halide ions. Such structure modification suppresses halide vacancy formation, thus leading to improved material properties. Compared to the GA-free perovskite reference samples, the optimal system $GA_{0.05}Cs_{0.15}FA_{0.8}Pb(I_{0.85}Br_{0.15})_3$ exhibits substantially improved thermal and photothermal stability, as well as increased photocarrier lifetime. Solar cells fabricated with the optimal material system show an excellent photovoltaic performance, with the champion device reaching a power conversion efficiency of 21.3% and an open circuit voltage of 1.229 V.

1. Introduction

Hybrid perovskites have recently emerged as a promising class of materials for efficient and cost-effective solar cells. Their excellent optoelectronic properties, which include a large absorption coefficient for visible light,[1] a large charge-carrier diffusion length,[2] and a small exciton binding energy,[3] have allowed for a rapid increase of the efficiency of hybrid perovskite solar cells from 3.8%[4] to a record 24.2%.[5] Hybrid lead halide perovskites have the chemical formula $APbX_3$, with A^+ cations, such as methylammonium (MA^+), formamidinium (FA^+) or Cs^+, filling the spaces between the PbX_6^{4-} octahedra (X^- = I^- or Br^-), which constitute a 3D network through corner-sharing.

Hybrid lead-perovskite structures suffer from various instabilities. The prototype compound, $MAPbI_3$, experiences a thermal instability due to the volatility of the organic cation MA^+.[6,7] Replacing MA^+ by a larger cation, such as FA^+, alleviates this problem, but it introduces a phase instability of forming photoinactive phase at room temperature, which is thought to be triggered by the larger cation severely distorting the perovskite structure.[8] Incorporating smaller alkali cations is a popular approach to address these instability issues. For instance, introducing a small amount of Cs^+ at the A^+ site of FA-perovskites has led to decent photovoltaic (PV) performance and improved stability.[9]

Besides the smaller Cs^+ cation, the large guanidinium (GA^+) cation has also been proposed as a promising candidate to substitute the A-site cation in hybrid perovskites.[10] It has been suggested via experimental studies that GA^+ can improve the perovskite's stability,[11] suppress the bias-induced ionic motion[10] and extend the charge-carrier lifetime.[12,13] GA^+ has an ionic radius of 278 pm; accordingly, the 3D-$GAPbI_3$ lattice has a Goldschmidt tolerance factor of 1.03 and is structurally unstable. However, by carefully controlling the film formation process, it is possible to mix GA^+ with MA^+ to form a phase stable 3D perovskite structure,[11,13] though the volatility of the remaining MA^+ may still induce thermal stability issues. Recent studies attempted to address the problem by incorporating GA^+ in a $FAPbI_3$ lattice, but the formed $GA_xFA_{1-x}PbI_3$ is also

Dr. Y. Zhou, Y.-H. Jia, Prof. N. Zhao
Department of Electronic Engineering
The Chinese University of Hong Kong
New Territories, Hong Kong
E-mail: nzhao@ee.cuhk.edu.hk

H. Xue, Prof. G. Brocks, Dr. S. Tao
Center for Computational Energy Research
Department of Applied Physics
Eindhoven University of Technology
5600 MB, Eindhoven, the Netherlands
E-mail: s.x.tao@tue.nl

Prof. G. Brocks
Computational Materials Science
Faculty of Science and Technology and MESA+
Institute for Nanotechnology
University of Twente
7500 AE, Enschede, the Netherlands

The ORCID identification number(s) for the author(s) of this article can be found under https://doi.org/10.1002/adfm.201905739.

DOI: 10.1002/adfm.201905739

thermodynamically unstable.[13,14] Replacing 17% of the FA^+ ions by the smaller Cs^+ cations, i.e., by using $FA_{0.83}Cs_{0.17}PbI_3$, was found to enable stable but limited (slight larger than 2 mol%) incorporation of GA^+ ions in the perovskite lattice.[15] On the other hand, up to 10 mol% GA^+ incorporation can be achieved by introducing a large amount of Br^- ions (>27 mol%) and Cs^+ ions (>32 mol%) in the lattice, yielding wide-bandgap ($E_g \geq 1.75$ eV) perovskite systems.[16] Clearly, the process of GA-incorporation is highly dependent on the lattice composition. Understanding the underlying mechanism that governs such dependence is important to achieve a stable and high PV efficiency perovskite system.

In this work we systematically study the possibility of substituting FA^+ cations in $FAPbI_3$ by GA^+ cations, while stabilizing the structure by a controlled amount of Cs^+ and Br^- substituting FA^+ and I^- ions respectively, without negatively affecting the optical properties of the original compound. Our champion compound, $GA_{0.05}Cs_{0.15}FA_{0.8}Pb(I_{0.85}Br_{0.15})_3$, has a bandgap of 1.625 eV. Density functional theory (DFT) calculations show that the presence of both Cs^+ and Br^- is critical to promote the GA^+ incorporation in the FA-based perovskite. Cs^+ and Br^- tend to occupy sites near each other, making room for the large cation GA^+ and reducing internal lattice strain. Detailed chemical bonding analysis demonstrates that once GA^+ is incorporated into the perovskite lattice, it forms strong H bonds with surrounding halide ions. As a result, the GA-incorporated perovskites show much improved thermal stability, increased carrier lifetime as well as suppressed halide segregation under thermal-photo stress. To experimentally evaluate the effectiveness of GA-incorporation, we have fabricated PV cells with an FTO/SnO_2/perovskite/Spiro-OMeTAD/Au device structure, and found that the hysteresis is highly suppressed and the open circuit voltage (V_{oc}) is increased after GA-incorporation. The champion PV device shows a stabilized power output (SPO)/V_{oc} of 20.5%/1.229 V, which are among the highest values reported in MA-free perovskites. Also, the GA-incorporated device can maintain 80% of its initial efficiency after 8 h operation at its maximum power output point under 1 sun illumination, in comparison to the device without GA only preserves 65%.

2. Results and Discussion

2.1. Structure of GA-Modified Perovskites

To systematically study how Cs^+ cation and Br^- anion substitutions affect the incorporation of GA^+ cations into a FA-based perovskite lattice, we consider the model compounds $FAPbI_3$, $FAPb(I_{0.85}Br_{0.15})_3$, $Cs_{0.15}FA_{0.85}PbI_3$, and $Cs_{0.15}FA_{0.85}Pb(I_{0.85}Br_{0.15})_3$. GA^+ ions are then introduced by adding a controlled amount of GABr (0, 3, 6, or 9 mol%) to the precursors. All perovskite thin films are prepared by the antisolvent method, using a SCN^--containing additive to achieve high crystallinity.[17] Note that the selection of GABr, rather than GAI, as the GA^+ source is important to elucidate the GA^+ incorporation effect, as the latter tends to introduce halide ion exchange and thus affect the lattice space and optical properties (Figure S1, Supporting Information). Also, when kept in a small amount, the excess Br^- (from GABr) could leave the perovskite system during annealing, as discussed in Figure S2 (Supporting Information), thus not affecting the original I:Br ratio of the system.

We use X-ray diffraction (XRD) to characterize the structures of the different compounds. In particular, incorporation of GA^+ ions in the perovskite structure is expected to result in an expansion of the lattice, due to the relatively large size of those ions. Such a lattice expansion leads to a shift of the perovskite XRD peaks toward a smaller angle. The XRD patterns of the four model compounds mentioned above, modified with addition of 0 to 9 mol% GABr, are shown in **Figure 1**. Below we discuss the possibility of incorporating GA^+ ions in the four model compounds one by one.

Focusing on the (002) diffraction peak of the 3D perovskite, Figure 1a shows that the (002) peak of $FAPbI_3$ stays almost unchanged at 28.08° after addition of GABr, which is a clear indication that GA^+ ions are not incorporated in the 3D perovskite lattice. Kubicki et al. have pointed out that addition of GA^+ to $FAPbI_3$ facilitates the formation of the optically inactive, low-dimensional phase (LDP) upon annealing.[13] We observe the emergence of the LDPs δ-$FAPbI_3$ and $FAGAPbI_4$[14,18] only in case a large amount of GABr (9 mol%) is added, see Figure 1c. This may be attributed to SCN^- in the precursor suppressing the formation of LDPs. Indeed, $FAPbI_3$ prepared without SCN^- yields a significant amount of LDPs upon addition of 3 mol% GABr, see Figure S3a (Supporting Information).

In the case of $FAPb(I_{0.85}Br_{0.15})_3$, a trigonal phase (TP) is observed before the introduction of GABr, in addition to the perovskite phase (Figure 1b), which is consistent with the results of a previous study.[19] After addition of 9 mol% GABr, the (002) peak of the perovskite phase shifts slightly from 28.30° to 28.28°, suggesting that a very small amount of GA^+ is incorporated in the perovskite lattice (Figure 1b). We also note the reduction of the TP and the formation of δ-$FAPbI_3$ and $FAGAPbI_4$[14,18] LDPs with increasing amounts of GABr (Figure 1b).

The (002) peak of $Cs_{0.15}FA_{0.85}PbI_3$ shows a monotonic shift from 28.19° to 28.17°, 28. 16° and 28.14° upon increasing the amount of GABr added from 0 to 3, 6 and 9 mol%, respectively (Figure 1c). This indicates that the presence of Cs^+ cations on the A-sites of the perovskite facilitates the incorporation of GA^+ ions. Based on the XRD data, we can estimate the amount of GA^+ incorporated in the $Cs_{0.15}FA_{0.85}PbI_3$ lattice. The detailed procedure of estimation is described in the Supporting Information and the results are summarized in **Table 1**. We find the actual GA^+ contents in the lattice are 1, 2, and 3 mol%, respectively, which are much smaller than the corresponding initial concentration of 3, 6, and 9 mol% of GA^+ (Table 1). Moreover, the photoinactive phase of δ-$FAPbI_3$ was found when GABr reached 9 mol%. Note that the same phenomenon was observed in a previous study,[15] which demonstrates a similar shift of 0.047° in the XRD main peak (≈28.2°), and the emergence of δ-$FAPbI_3$ with addition of 10 mol% GA^+ in the $FA_{0.83}Cs_{0.17}PbI_3$ perovskite. These results may indicate the incorporation of ≈3 mol% GA^+ (with addition of ≈10 mol% GA-salt) ions in the $Cs_{0.15}FA_{0.85}PbI_3$ perovskite lattice has reached the upper limit of sustaining a stable 3D structural.

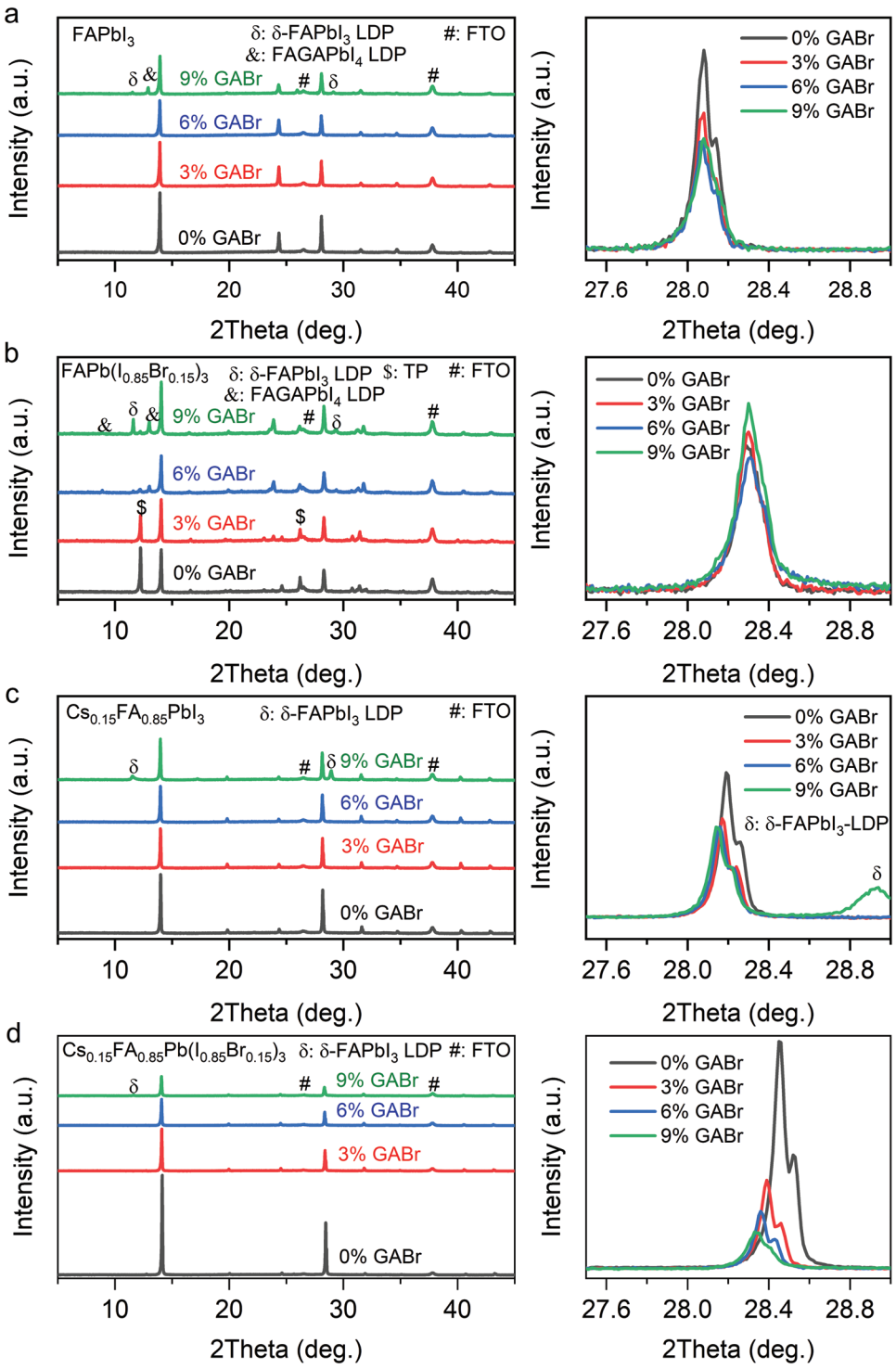

Figure 1. XRD patterns of a) $FAPbI_3$, b) $FAPb(I_{0.85}Br_{0.15})_3$, c) $Cs_{0.15}FA_{0.85}PbI_3$, and d) $Cs_{0.15}FA_{0.85}Pb(I_{0.85}Br_{0.15})_3$ perovskite thin films prepared with precursors containing 0 to 9 mol% GABr additive. The figures on the right zoom in on the (002) diffraction peak.

Finally, for $Cs_{0.15}FA_{0.85}Pb(I_{0.85}Br_{0.15})_3$, where both Br^- anions and Cs^+ cations are introduced in the perovskite lattice, the (002) peak demonstrates a far more prominent shift from 28.45° to 28.39°, 28. 36° and 28.34° with the addition of GABr increasing from 0 to 3, 6 and 9 mol%, respectively (Figure 1d). It is clear that the presence of both Br^- and Cs^+ in the lattice significantly enhances the incorporation of GA^+. Moreover, the $FAGAPbI_4$ LDP is not formed here, which is another indication of the more efficient incorporation of GA^+ in the 3D perovskite phase. We also estimated the content of GA^+

Table 1. Calculated GA^+ concentrations in $Cs_{0.15}FA_{0.85}PbI_3$ and $Cs_{0.15}FA_{0.85}Pb(I_{0.85}Br_{0.15})_3$ prepared with precursors containing GABr.

GABr [mol%]		0	3	6	9
$Cs_{0.15}FA_{0.85}PbI_3$	Peak [°]	28.19	28.17	28.16	28.14
	GA [mol%]	0	1	2	3
$Cs_{0.15}FA_{0.85}Pb(I_{0.85}Br_{0.15})_3$	Peak [°]	28.45°	28.39°	28.36°	28.34°
	GA [mol%]	0	3	5	6

incorporation in this case through XRD peak shift (details are shown in the Supporting Information and results are summarized in Table 1), and the results show the GA^+ incorporation is significantly enhanced to 3, 5, and 6 mol% when compared with $Cs_{0.15}FA_{0.85}PbI_3$ by adding 3, 6, and 9 mol% GABr, respectively (Table 1). Again, the photoinactive phase is formed when the addition of GABr reaches 9 mol% (expansion of the XRD signal of the photoinactive phase is shown in Figure S4a, Supporting Information). After comparing the results with the reported XRD patterns (both experimental[15] and simulated ones[20]) and also the reference pattern of mixed δ- and α-$FAPbI_3$ (Figure S4b, Supporting Information)), we speculate that the peak may correspond to a δ-$FAPbI_3$ phase containing a small amount of Br and/or Cs. (The phase has a peak position of ≈11.6° while pure δ-$FAPbI_3$ has a peak at ≈11.5°.) It is also worth noting that the (002) peak intensity decreases with the increasing addition of GABr. We attribute this result to the reduction in the crystal grain size from (1.2 ± 0.11) µm for the 0 mol% GABr sample to (1.05 ± 0.10) µm, (0.97 ± 0.08) µm and (0.95 ± 0.07) µm for the 3, 6, and 9 mol% GABr samples, respectively (Figure S5, Supporting Information).

2.2. Atomistic Model of GA^+ Incorporation

To understand the role of Cs^+ and Br^- in the incorporation of GA^+ in FA-based perovskite, we perform DFT calculations. The exact stoichiometries as they are used in experiment would require calculations on prohibitively large supercells, so we adapted the stoichiometries somewhat, such that all calculations can be done with a (2 × 2 × 2) $FAPbI_3$ supercell. We created relevant structural models by replacing one FA^+ cation and/or three I^- anions in a supercell by one GA^+ and/or one Cs^+ cation and/or three Br^-.After testing dozens of configurations (see Table SIII, Supporting Information), we select the most stable structures of all relevant perovskites. The most stable structures of $GA_{1/8}FA_{7/8}Pb(I_{7/8}Br_{1/8})_3$, $GA_{1/8}Cs_{1/8}FA_{3/4}PbI_3$ and $GA_{1/8}Cs_{1/8}FA_{3/4}Pb(I_{7/8}Br_{1/8})_3$ are displayed in **Figure 2**a–c; those of $GA_{1/8}FA_{7/8}PbI_3$, $Cs_{1/8}FA_{7/8}PbI_3$, $FAPb(I_{7/8}Br_{1/8})_3$, and $Cs_{1/8}FA_{7/8}Pb(I_{7/8}Br_{1/8})_3$ are shown in Figure S6 (Supporting Information).

Our starting point is that, in principle, $FAPbI_3$ should be suited to incorporate GA^+, as the FA^+ and GA^+ ions are similar in size. However, as shown in the previous section, the intrinsic

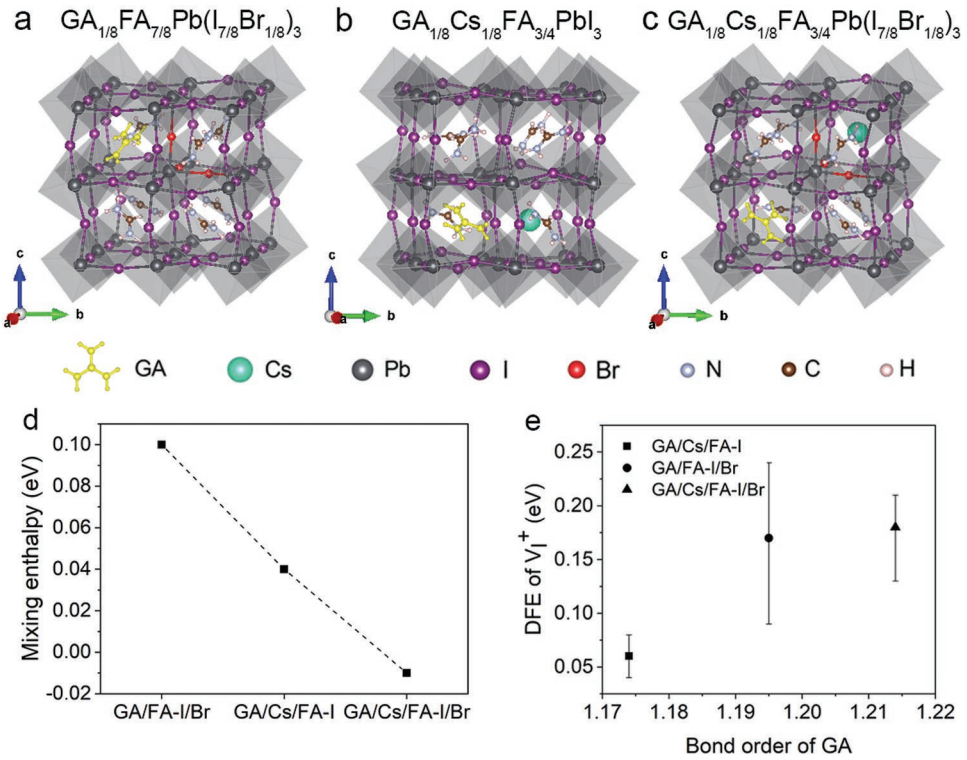

Figure 2. DFT optimized structures of a) $GA_{1/8}FA_{7/8}Pb(I_{7/8}Br_{1/8})_3$, b) $GA_{1/8}Cs_{1/8}FA_{3/4}PbI_3$, and c) $GA_{1/8}Cs_{1/8}FA_{3/4}Pb(I_{7/8}Br_{1/8})_3$, denoted as GA/FA/-I/Br, GA/Cs/FA-I, and GA/Cs/FA-I/Br, respectively; d) Enthalpy of GA incorporation, see Equation (1); e) defect formation energy (DFE) of iodine vacancies (V_I^+) versus the total bond order of the GA^+ cation with surrounding inorganic framework. The DFE is calculated with respect to the DFE in pure $FAPbI_3$. The vertical lines represent the DFE range for different lattice positions of V_I^+; the data point represents the average (see Table SIV, Supporting Information).

instability of $FAPbI_3$ against formation of the nonperovskite yellow phase is only enhanced by GA^+. Therefore, in order to stabilize $FAPbI_3$, one first needs to incorporate Cs^+ and/or Br^- ions. To evaluate how easy it is to incorporate GA^+ in these modified perovskites, we calculate the enthalpy defined as

$$\Delta H = E\left[GA_xCs_yFA_{1-x-y}Pb(I_{1-z}Br_z)_3\right] - E\left[Cs_yFA_{1-y}Pb(I_{1-z}Br_z)_3\right] - E\left[GA_xFA_{1-x}PbI_3\right] + E\left[FAPbI_3\right] \quad (1)$$

where $E[...]$ are the DFT total energies of the corresponding compounds (with optimized cell volumes) per supercell. ΔH describes the change in enthalpy when GA^+ is incorporated in $Cs_yFA_{1-y}Pb(I_{1-z}Br_z)_3$, compared to the enthalpy change when GA^+ is incorporated in pure $FAPbI_3$. The results shown in Figure 2d show that ΔH is positive for $y=\frac{1}{8}; z=0$ and for $y=0; z=\frac{1}{8}$, i.e., if next to GA^+ either Cs^+ or Br^- ions are incorporated. The positive enthalpies indicate that it is difficult to incorporate GA^+, in agreement with experimental observation that only about 1% to 2% of GA is incorporated in these compounds. In contrast, ΔH is slightly negative for $y=\frac{1}{8}; z=\frac{1}{8}$, i.e., if next to GA^+ both Cs^+ and Br^- ions are incorporated. These findings are in agreement with the experimental finding that incorporation of GA^+ is enhanced when Cs^+ and Br^- are both present in the $FAPbI_3$ perovskite.

To clarify the atomistic origin of the enhanced incorporation of GA^+ we carefully examined the local structures (Figure S7, Supporting Information) of $GA_xCs_yFA_{1-x-y}Pb(I_{1-z}Br_z)_3$. Direct incorporation of 12.5% of GA $\left(x=\frac{1}{8}\right)$ in $FAPbI_3$ leads to a slight volume expansion of 0.5%. This increase of volume likely contributes to the instability of the lattice, which for $FAPbI_3$ is already strained because of the relatively large size of the FA^+ ion. Further incorporation of Br^- $\left(z=\frac{1}{8}\right)$ or Cs^+ $\left(y=\frac{1}{8}\right)$ decreases the lattice volume slightly, i.e., by 1.3% and 0.5% respectively. Interestingly, although the lattice volumes of $GA_{1/8}FA_{7/8}Pb(I_{7/8}Br_{1/8})_3$ and $GA_{1/8}Cs_{1/8}FA_{3/4}PbI_3$ become slightly smaller, the average bond length between the Pb^{2+} and I^- ions surrounding the GA^+ ion increases, i.e., by 0.021 and 0.027 Å, respectively (Figure S7b, Supporting Information).

The two opposite trends point toward a general observation: small ions, such as Br^- or Cs^+, occupy a relatively small space in the perovskite lattice, and make room for the large GA^+ cation. The effects become even more pronounced if we incorporate all of these ions, in $GA_{1/8}Cs_{1/8}FA_{3/4}Pb(I_{7/8}Br_{1/8})_3$, as evidenced by the smallest perovskite lattice volume and largest Pb—I bond lengths around GA sites (Figure S7, Supporting Information). The lowest energy structure of this compound has a special atomic configuration (Figure 2c), where three Br^- anions form one facet of a octahedron that pulls the nearby Cs^+ action away from its A site, leaving sufficient room in the opposite diagonal direction for the nearby GA^+ cation.

The above structural analysis is further supported by a chemical bonding analysis (Figure S8, Supporting Information). Of all compounds studied, the total bond order of GA^+, a measure of covalent bond strength, is largest in $GA_{1/8}Cs_{1/8}FA_{3/4}Pb(I_{7/8}Br_{1/8})_3$, indicating that the interactions of GA^+ with the surrounding inorganic framework are strongest in this compound. The strong GA-halide interaction is expected to have a positive effect on suppressing halide defects. Indeed, DFT calculated defect formation energies of iodine vacancies show a substantial increase by 0.18 eV on average for $GA_{1/8}Cs_{1/8}FA_{3/4}Pb(I_{7/8}Br_{1/8})_3$ compared to the same defect formation energies in the reference perovskite $FAPbI_3$ (Figure 2e and Table SIV, Supporting Information).

2.3. Tests on Material's Stability

Having established that both Cs^+ and Br^- are required to successfully incorporate GA^+ in a $FAPbI_3$-based perovskite, we focus on the experimental composition $Cs_{0.15}FA_{0.85}Pb(I_{0.85}Br_{0.15})_3$, and denote the compounds $GA_xCs_{0.15}FA_{0.85-x}Pb(I_{0.85}Br_{0.15})_3$ ($x = 0$, 0.03, 0.05, and 0.06) by GA_x in the following.

We conduct thermal stability tests of GA_0 and $GA_{0.05}$ perovskite thin films by heating them and keeping them at 130 °C for 10 h in a N_2-filled glovebox. For the GA_0 sample (containing no GA^+), a signal emerges in the XRD pattern that can be attributed to PbI_2 (Figure S9, Supporting Information), indicating decomposition of the perovskite compound. In contrast, the $GA_{0.05}$ sample shows no such PbI_2 signal (Figure S9, Supporting Information), which indicates a much-improved thermal stability.

We then perform an accelerated aging test with the GA_0 and $GA_{0.05}$ perovskite thin films by exposing them to continuous 200 mW cm^{-2} white light-emitting diode (LED) illumination for 10 h at 110 °C. This test is performed because halide segregation is often observed when mixed I–Br perovskites are exposed to simultaneous photo and thermal stress,[21] which is a common scenario in the practical operation of solar cells. We find that the aged GA_0 perovskite thin film exhibits a reduced intensity and an evident broadening of XRD peaks (**Figure 3**a), evidencing a degraded crystallinity that is likely associated with a more defective crystal lattice.

Moreover, XRD peaks also shift toward lower angles, which suggests the segregation of a Br-rich phase from the original GA_0 perovskite (Figure 3a). The above observation is confirmed by the PL spectra, where the aged GA_0 sample (Figure 3b) shows a broadening and redshift of peaks, the latter corresponding to a longer-wavelength emission from an I-rich phase. In contrast, the aged $GA_{0.05}$ sample shows much less severe degradation (Figure 3c,d).

From our aging tests we conclude that incorporation of GA^+ suppresses halide segregation, as well as degradation of perovskite materials overall, improving the thermal and thermal-photostability of the perovskite material.

2.4. Optoelectronic Properties and Photovoltaic Performance

To evaluate in more detail the impact of the incorporation of GA^+ on the optical properties of the perovskite materials, we measure the ultraviolet–visible (UV–vis) absorption and PL spectra of the GA_x ($x = 0$, 0.03, 0.05, and 0.06) compounds. The absorption onset for all perovskites remains almost unchanged at 1.625 eV, as determined from the Tauc plots (**Figure 4**a), which indicates incorporation of GA^+ within 6 mol% has barely

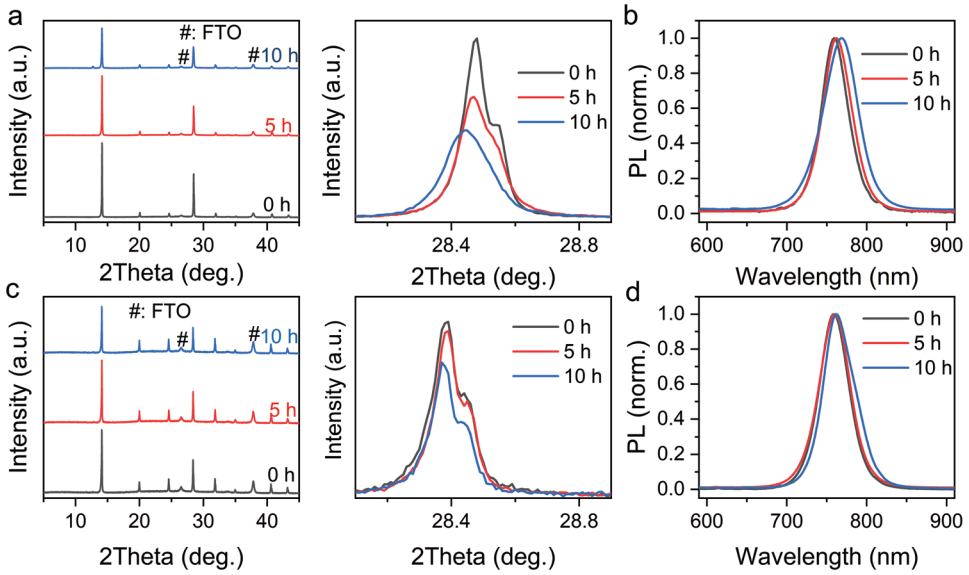

Figure 3. XRD patterns of the a) GA_0 and c) $GA_{0.05}$ perovskite thin films aged under a white LED with a light intensity of 200 mW cm^{-2} for 0, 5, and 10 h at 110 °C; PL spectra of the b) GA_0 and d) $GA_{0.05}$ perovskite thin films aged under the same conditions.

any impact on the bandgap. The absorption spectrum shows little change for x from 0 to 0.05, but the absorbance drops notably for $x = 0.06$ (Figure 4a). This reduction in absorbance is possibly due to the formation of δ-$FAPbI_3$[15] at such high GA^+ concentrations (Figure S4, Supporting Information).

The PL spectra of the GA_x perovskites in Figure 4b show no changes in peak positions for all x values ($x = 0$, 0.03, 0.05, and 0.06), consistent with the unchanged absorption onset. Interestingly, the emission intensity is enhanced significantly with increasing of x, indicating the incorporation of GA^+ suppresses nonradiative recombination. A reduction of nonradiative recombination is confirmed by the time-resolved PL (TRPL) decay in Figure 4c, where the PL lifetime increases from 19.27 to 98.10 ns continuously with x going from 0 to 0.06.

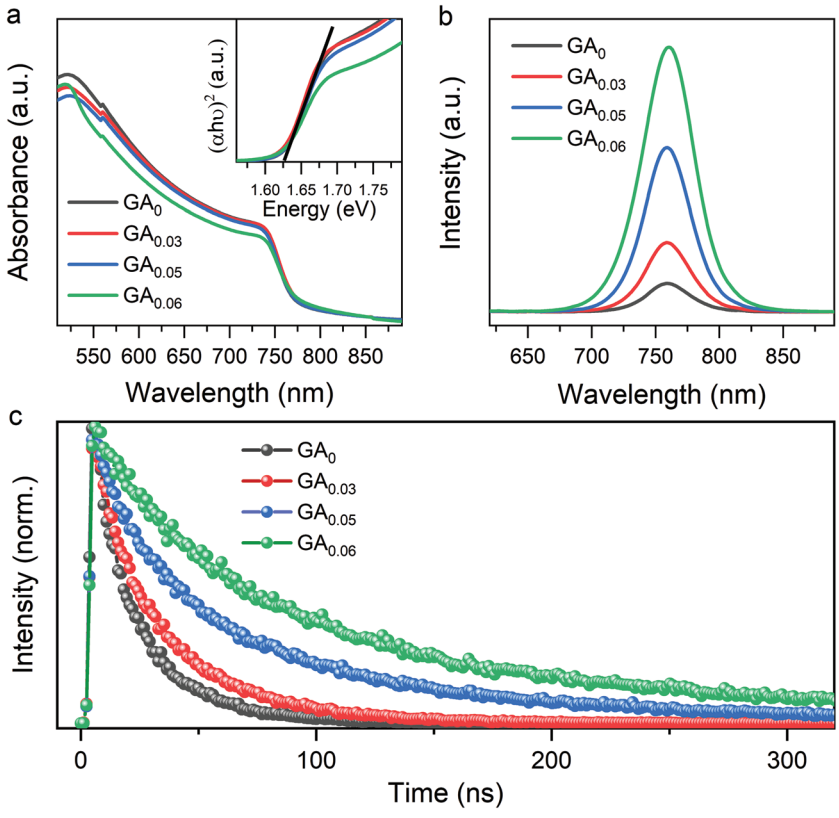

Figure 4. a) Absorption spectra of GA_x perovskite thin films with $x = 0$, 0.03, 0.05, and 0.06; b) PL spectra and c) TRPL spectra.

It is well known that halide vacancies commonly exist in perovskite materials due to their low formation energy.[22,23] A recent study suggests that it is possible to deoxidize such defects under light illumination and transform them from shallow to deep traps.[24] The improved carrier lifetime we find is then consistent with the suppression of such halide defects, as indicated by our DFT results of the increased halide vacancy formation energy (Figure 2e).

Finally, we evaluate the PV performance of the GA_x (x = 0, 0.03, 0.05, and 0.06) perovskites in the device structure FTO/SnO_2/GA_x/Spiro-MeOTAD/Au. The statistics of the PV parameters are summarized in **Figure 5**a. It can be seen that the V_{oc} of the devices increases with increasing x, which may be associated with the suppressed nonradiative recombination upon incorporation of GA^+. Moreover, hysteresis in the devices, i.e., the difference in the PV parameters between the forward scan (FS) and backward scan (BS), is reduced with increasing x, which is possible due to both the improved carrier charge

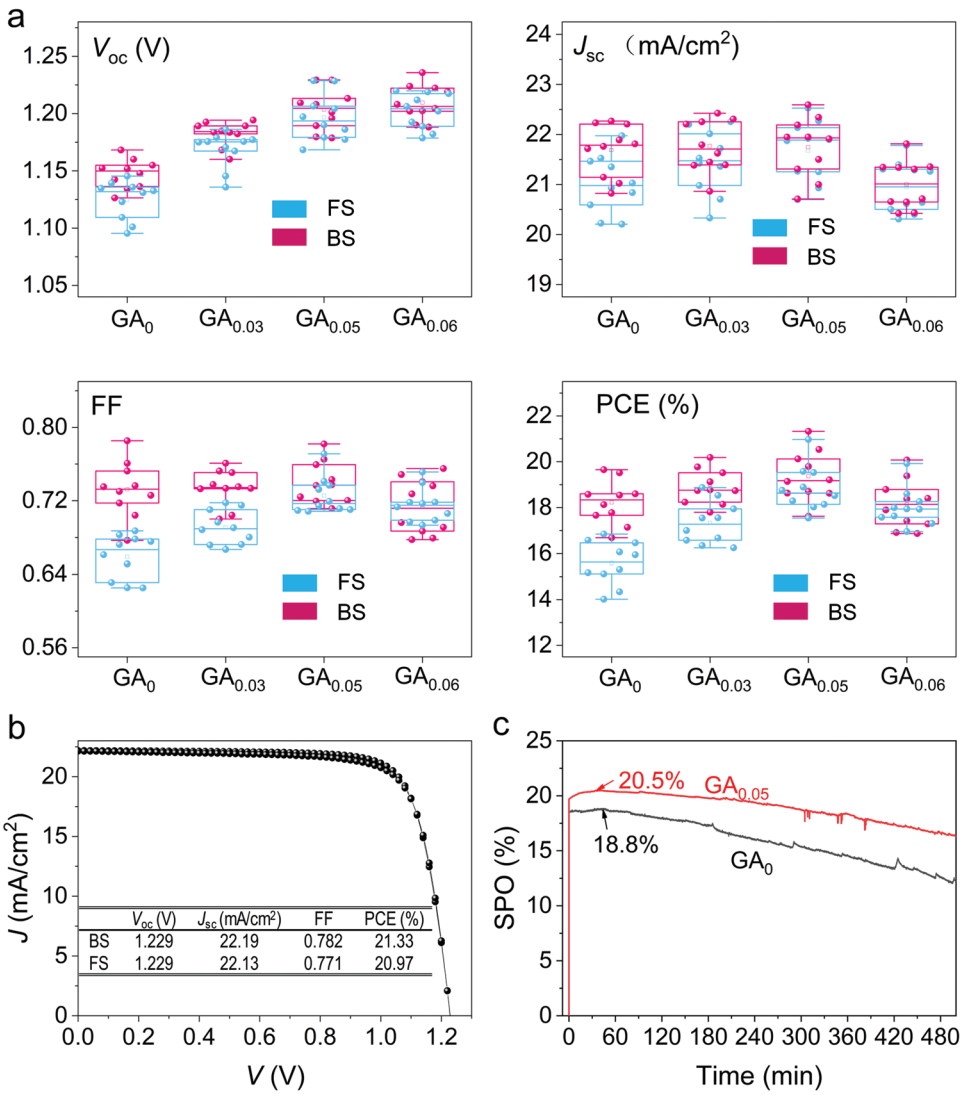

Figure 5. a) Statistics of the photovoltaic parameters of the solar cells fabricated from GA_x perovskite thin films ($x = 0$, 0.03, 0.05, and 0.06); b) Current density–Voltage (J–V) curve of the champion device fabricated from $GA_{0.05}$ perovskite; c) Comparison of the stabilized power outputs (SPOs) of the devices fabricated from GA_0 and $GA_{0.05}$ perovskite thin films. The devices are tested under 1 sun illumination at maximum power output point in N_2 atmosphere.

transport[15] and suppressed ion migration upon GA^+ incorporation. The short-circuit current density (J_{sc}) is approximately constant for all x up to 0.05. The $GA_{0.06}$ perovskite-based solar cells in general show a reduction in J_{sc}, consistent with the lower absorbance of $GA_{0.06}$ due to the presence of the photoinactive LDP phase in this compound.

The optimal PV performance is obtained for the $GA_{0.05}$ perovskite, with the champion device demonstrating an efficiency of 21.33% and a V_{oc} of 1.229 V in the BS (Figure 5b). We then trace the stabilized power output of the GA_0- and $GA_{0.05}$-based devices under 1 sun illumination at their maximum power output point. As shown in Figure 5c, the $GA_{0.05}$ device maintains 80% of the initial efficiency after 8 h operation, while the GA_0 device only preserves 65% of its initial efficiency. We also summarize the reported PV metrics of GA-incorporated perovskites with bandgap lower than 1.65 eV in Table SV (Supporting Information), which demonstrates the majority of the literature reported the incorporation of GA^+ in MA-containing perovskites; while ref. [15] and our work focus on the incorporation of GA^+ in FA-based perovskites. By optimizing GA^+ content, we demonstrate the solar cell based on $GA_{0.05}Cs_{0.15}FA_{0.8}Pb(I_{0.85}Br_{0.15})_3$ perovskite to be one of the most efficient with the lowest open circuit loss.

3. Conclusions

In conclusion, we have demonstrated a highly reproducible method for incorporating GA^+ in FA-based perovskites for efficient and stable perovskite solar cells. The key factor to this is the simultaneous incorporation of limited amounts of Cs^+ and Br^-, which synergistically enhance the

incorporation of GA^+ into the perovskite lattice. Once GA^+ cation is successfully incorporated, it binds the surrounding halides more tightly than FA^+ does, and therefore improves the structural stability and increases the formation energy of halide vacancies. Accordingly, the GA-modified perovskite films show a significant increase in carrier lifetime and the thermal-photostability.

Remarkably, solar cells made of GA-modified perovskite also show a reduced hysteresis and an improved PV performance. The optimal PV performance is obtained for the perovskite with composition $GA_{0.05}Cs_{0.15}FA_{0.8}Pb(I_{0.85}Br_{0.15})_3$, with the champion device reaching a power conversion efficiency of 21.3%, a SPO of 20.5% and a V_{oc} of 1.229 V. This solar cell also demonstrates improved operational stability, maintaining 80% of its initial efficiency after 8 h operation at its maximum power output point under 1 sun illumination, while a device based upon GA_0 perovskite only preserves 65%. This study provides an important insight in the synergistic role of Cs^+ and Br^- in the successful incorporation of GA^+ in FA-based perovskite and points to a promising route for the fabrication of MA-free perovskite solar cells with high stability and high PV performance.

4. Experimental Section

Substrate Cleaning: Nippon Sheet Glass was cleaned by sonication in a 2% Hellmanex water solution for 30 min. After rinsing with deionized water and ethanol, the substrates were further cleaned with isopropanol, acetone and isopropanol for 30 min, respectively. The substrates were then dried and stored in a dry box with the humidity controlled under 30% RH.

Preparation of SnO_2 Films: The SnO_2 colloid precursor was obtained from Alfa Aesar (tin(IV) oxide, 15% in H_2O colloidal dispersion). Before use, the SnO_2 colloid precursor was mixed with water in a volume ration of 1:5.67. The FTO substrates were treated by UV–ozone for 15 min before depositing of SnO_2. The diluted SnO_2 colloid solution was spin coated onto FTO substrates at 3000 rpm for 30 s, and then baked on a hotplate in ambient air (humidity around 70% RH, temperature around 22 °C) at 120 °C for 10 min, followed by 30 min at 180 °C. After annealing, the hotplate was switched off, and the FTO substrates were allowed to cool down to room temperature naturally. Subsequently, the substrates were treated by UV–ozone one more time for 15 min and then transferred to a glovebox.

Preparation of Perovskite Films: A solution of $(CsI)_{0.15}(FAI)_{0.85}(PbI_2)_{0.775}(PbBr_2)_{0.225}$ was prepared by mixing 0.15 M CsI (Dyesol), 0.85 M FAI (Dyesol), 0.775 M PbI_2 (TCI, 99.999%), and 0.225 M $PbBr_2$ (TCI, 99.999%) in anhydrous DMF: DMSO 4:1 (v:v) and stirred overnight (denoted as solution A). Solutions of $(CsI)_{0.15}(FAI)_{0.85}[Pb(SCN)_2 + 2FAI]_{0.775}[Pb(SCN)_2 + 2FABr]_{0.225}$ were prepared by mixing 0.15 M CsI (Dyesol), 2.4 M FAI (Dyesol), 0.45 M FABr (Dyesol), and 1 M $Pb(SCN)_2$ (Sigma-Aldrich, 99.999%) in anhydrous DMF: DMSO 4:1 (v:v) and stirred overnight (denoted as solution B). A solution of GABr was prepared by dissolving 1 M GABr (Dyesol, 99.999%) in anhydrous DMF: DMSO 4:1 (v:v) and stirred overnight. The precursor used for perovskite deposition was prepared by mixing solution A and solution B in a volume ratio of 10:1 first, followed by adding y vol% GABr solution (y = 0, 3, 6, and 9). The precursor solutions were spin-coated onto the glass or SnO_2/FTO substrates in a two-step procedure at 1000 and 4000 rpm for 10 and 40 s respectively. During the second step, 120 µL of chlorobenzene was casted onto the substrates 10 s before the ending of the second spinning step. The films were placed on a hotplate at 100 °C for 60 min. The preparation of perovskite thin films was performed in a N_2-purged glovebox.

Preparation of Hole Transport Layer and Au Electrode: The hole-transport layer precursor was prepared by dissolving 72.3 mg spiro-MeOTAD (TRC, Canada), 28 µL 4-*tert*-butylpyridine (Sigma-Aldrich, 96%) and 17.5 µL bis(trifluoromethane)sulfonimide lithium salt (Sigma-Aldrich) solution (520 mg Li-TFSI in 1 mL acetonitrile) in 1 mL chlorobenzene. The precursor was then spin-coated on the perovskite layer at 4000 rpm for 30 s. The deposition of the hole transport layer was in glovebox. The solar cells were then transferred to a box with dry air (humidity lower than 20% RH) for oxidation for 16 h. Finally, a 100 nm Au electrode layer was deposited under a vacuum of $<1 \times 10^{-4}$ Pa with a rate of 0.1 nm s^{-1}. The preparation of the Au electrode was performed in a N_2-purged glovebox.

Measurement and Characterization: The film morphology was characterized using scanning electron microscopy (SEM, Quanta 400). The XRD patterns of the samples were recorded using a Rigaku RU-300 diffractometer equipped with Cu Kα_1 irradiation (λ = 1.5406 Å). Ultraviolet–visible absorption spectra were taken on a Hitachi U-3501 ultraviolet/visible/near-infrared spectrophotometer. The PL spectra were measured with an AvaSpec ULS2048 × 64 (Avantes) spectrometer, using excitation by 405 nm light source. The thermal stability test was performed on a hotplate with the temperature fixed at 130° in glovebox. The photothermal stress test was conducted under a white LED with an intensity of 200 mW cm^{-2}, keeping the temperature at 85 °C in glovebox. Time-resolved photoluminescence measurements were performed by exciting the samples with the second harmonic (400 nm) of a mode-locked femtosecond Ti:Sapphire laser with a repetition rate of 76 MHz (Mira 900, Coherent). The excitation density was reduced to be 1.4 µJ cm^{-2} by a neutral density filter. The spectra were detected using a Hamamatsu streak camera, working on the single sweep mode. The repetition rate of excitation was reduced by a pulse picker. The current density–voltage (J–V) curves were measured under simulated AM 1.5 one-sun illumination (100 mW cm^{-2}, 94011A-ES, ABB). The light intensity was adjusted using a Newport calibrated Si solar cell (91 150-KG5, Newport). The mismatch factor was calculated to be less than 1.5%. The active area of the solar cell was 0.05 cm^2, as determined by optical microscope. The forward J–V scans were measured from forward bias to short-circuit and the backward scans were from short-circuit to forward bias, both at a scan rate of 100 mV s^{-1}. All the devices are biased at 1.3 V at 1 sun illumination for 10 s before measurement.

Computational Methods: Density functional theory calculations were performed at the level of the generalized gradient approximation (GGA) in the Perdew–Burke–Ernzerhof (PBE) parameterization,[24,25] as implemented in the Vienna ab initio simulation package (VASP).[26–28] The cell volume and positions of the ions were fully relaxed during geometry optimization. An energy cutoff of 500 eV and 3 × 3 × 3 k-point meshes were used. The energy and force convergence criteria were set to 10^{-5} eV and 5 meV $Å^{-1}$, respectively. For simulations of complex perovskite alloys, a 2 × 2 × 2 supercell of $FAPbI_3$ perovskite (cubic unit cell with lattice parameter a = 6.45 Å) was used as a starting structure, where different structures were created by replacing one FA^+ cation and/or three I^- anions by one GA^+ and/or one Cs^+ cation and three Br^- anions, respectively. Details of all configurations are given in Table SIII (Supporting Information). Spin–orbit coupling (SOC) was included in the self-consistent calculations based on the equilibrium structures.[29]

The density derived electrostatic and chemical (DDEC6) method[30–32] was used to calculate the total bond order of chemical bonds associated with the interaction of the GA^+ cation with the surrounding Pb and I atoms. A larger value indicates a stronger covalent interaction.

The relative defect formation energy[33,34] of iodine vacancies (V_I^+) in GA-based perovskites with respect to those in the reference perovskite $FAPbI_3$ were calculated according to the following equation

$$\Delta H_f\left[V_I^+, GA\right] = \left\{E\left[V_I^+, GA\right] - E\left[\text{bulk}, GA\right]\right\} - \left\{E\left[V_I^+, FAPbI_3\right] - E\left[\text{bulk}, FAPbI_3\right]\right\} \quad (2)$$

where ΔH_f is the defect formation energy; $E[V_I^+]$ and E[bulk] are the DFT total energies of defective and pristine supercells, respectively.

Supporting Information

Supporting Information is available from the Wiley Online Library or from the author.

Acknowledgements

Y.Z. and H.X. contributed equally to this work. The authors gratefully acknowledge the fundings from the General Research Fund (Ref No: CUHK 14210917) and the Theme-based Research Scheme (Grant No. T23-407/13-N) from the Research Grants Council of Hong Kong. H.X. acknowledges the funding from the China Scholarship Council (CSC). S.T. acknowledges funding by the Computational Sciences for Energy Research (CSER) tenure track program of Shell and NWO (Project number 15CST04-2), the Netherlands.

Conflict of Interest

The authors declare no conflict of interest.

Keywords

DFT calculations, guanidium incorporation, hysteresis, methylammonium-free

Received: July 16, 2019
Revised: August 25, 2019
Published online: September 19, 2019

[1] S. De Wolf, J. Holovsky, S. Moon, P. Löper, B. Niesen, M. Ledinsky, F. Haug, J. Yum, C. Ballif, *J. Phys. Chem. Lett.* **2014**, *5*, 1035.
[2] S. D. Stranks, G. E. Eperon, G. Grancini, C. Menelaou, M. J. Alcocer, T. Leijtens, L. M. Herz, A. Petrozza, H. J. Snaith, *Science* **2013**, *342*, 341.
[3] G. Xing, N. Mathews, S. Sun, S. S. Lim, Y. M. Lam, M. Grätzel, S. Mhaisalkar, T. C. Sum, *Science* **2013**, *342*, 344.
[4] A. Kojima, K. Teshima, Y. Shirai, T. Miyasaka, *J. Am. Chem. Soc.* **2009**, *131*, 6050.
[5] Best Research-Cell Efficiencies, https://www.nrel.gov/pv/assets/pdfs/best-research-cell-efficiencies.20190802.pdf (accessed: June 2019).
[6] B. Conings, J. Drijkoningen, N. Gauquelin, A. Babayigit, J. D'Haen, L. D'Olieslaeger, A. Ethirajan, J. Verbeeck, J. Manca, E. Mosconi, *Adv. Energy Mater.* **2015**, *5*, 1500477.
[7] S. Wang, Y. Jiang, E. J. Juarez-Perez, L. K. Ono, Y. Qi, *Nat. Energy* **2017**, *2*, 16195.
[8] C. C. Stoumpos, C. D. Malliakas, M. G. Kanatzidis, *Inorg. Chem.* **2013**, *52*, 9019.
[9] C. Yi, J. Luo, S. Meloni, A. Boziki, N. Ashari-Astani, C. Grätzel, S. M. Zakeeruddin, U. Röthlisberger, M. Grätzel, *Energy Environ. Sci.* **2016**, *9*, 656.
[10] G. Giorgi, J. Fujisawa, H. Segawa, K. Yamashita, *J. Phys. Chem. C* **2015**, *119*, 4694.
[11] A. D. Jodlowski, C. Roldán-Carmona, G. Grancini, M. Salado, M. Ralaiarisoa, S. Ahmad, N. Koch, L. Camacho, G. de Miguel, M. K. Nazeeruddin, *Nat. Energy* **2017**, *2*, 972.
[12] N. D. Marco, H. Zhou, Q. Chen, P. Sun, Z. Liu, L. Meng, E. Yao, Y. Liu, A. Schiffer, Y. Yang, *Nano Lett.* **2016**, *16*, 1009.
[13] D. J. Kubicki, D. Prochowicz, A. Hofstetter, M. Saski, P. Yadav, D. Bi, N. Pellet, J. Lewiński, S. M. Zakeeruddin, M. Grätzel, L. Emsley, *J. Am. Chem. Soc.* **2018**, *140*, 3345.
[14] O. Nazarenko, M. R. Kotyrba, S. Yakunin, M. Aebli, G. Rainò, B. M. Benin, M. Wörle, M. V. Kovalenko, *J. Am. Chem. Soc.* **2018**, *140*, 3850.
[15] N. D. Pham, C. Zhang, V. T. Tiong, S. Zhang, G. Will, A. Bou, J. Bisquert, P. E. Shaw, A. Du, G. J. Wilson, H. Wang, *Adv. Funct. Mater.* **2019**, *29*, 1806497.
[16] R. J. Stoddard, A. Rajagopal, R. L. Palmer, I. L. Braly, A. K. Y. Jen, H. W. Hillhouse, *ACS Energy Lett.* **2018**, *3*, 1261.
[17] Y. Zhou, Y. Jia, H. Fang, M. A. Loi, F. Xie, L. Gong, M. Qin, X. Lu, C. Wong, N. Zhao, *Adv. Funct. Mater.* **2018**, *28*, 1803130.
[18] W. Zhang, J. Xiong, J. Li, W. A. Daoud, *J. Mater. Chem. A* **2019**, *7*, 9486.
[19] D. P. McMeekin, G. Sadoughi, W. Rehman, G. E. Eperon, M. Saliba, M. T. Hörantner, A. Haghighirad, N. Sakai, L. Korte, B. Rech, *Science* **2016**, *351*, 151.
[20] O. Nazarenko, M. R. Kotyrba, M. Wörle, E. Cuervo-Reyes, S. Yakunin, M. V. Kovalenko, *Inorg. Chem.* **2017**, *56*, 11552.
[21] Y. Zhou, F. Wang, Y. Cao, J. P. Wang, H. H. Fang, M. A. Loi, N. Zhao, C. P. Wong, *Adv. Energy Mater.* **2017**, *7*, 1701048.
[22] A. Buin, P. Pietsch, J. Xu, O. Voznyy, A. H. Ip, R. Comin, E. H. Sargent, *Nano Lett.* **2014**, *14*, 6281.
[23] W. Yin, T. Shi, Y. Yan, *Appl. Phys. Lett.* **2014**, *104*, 063903.
[24] W. Li, Y. Sun, L. Li, Z. Zhou, J. Tang, O. V. Prezhdo, *J. Am. Chem. Soc.* **2018**, *140*, 15753.
[25] K. Burke, M. Ernzerhof, J. P. Perdew, *Phys. Rev. Lett.* **1996**, *77*, 3865.
[26] J. Hafner, G. Kresse, *Phys. Rev. B* **1993**, *47*, 558.
[27] G. Kresse, J. Furthmüller, *Comput. Mater. Sci.* **1996**, *6*, 15.
[28] J. Furthmüller, G. Kresse, *Phys. Rev. B* **1996**, *54*, 11169.
[29] J. Even, L. Pedesseau, J. Jancu, C. Katan, *J. Phys. Chem. Lett.* **2013**, *4*, 2999.
[30] T. A. Manz, N. G. Limas, *RSC Adv.* **2016**, *6*, 47771.
[31] T. A. Manz, *RSC Adv.* **2017**, *7*, 45552.
[32] C. Onwudinanti, I. Tranca, T. Morgan, S. Tao, *Nanomaterials* **2019**, *9*, 129.
[33] C. G. Van de Walle, J. Neugebauer, *J. Appl. Phys.* **2004**, *95*, 3851.
[34] D. Meggiolaro, F. De Angelis, *ACS Energy Lett.* **2018**, *3*, 2206.